The *Virga-Sniffer* - a new tool to identify precipitation evaporation using ground-based remote-sensing observations

Heike Kalesse-Los[1], Anton Kötsche[1], Andreas Foth[1], Johannes Röttenbacher[1], Teresa Vogl[1], and Jonas Witthuhn[1]

[1]Leipzig Institute for Meteorology (LIM), University of Leipzig, Leipzig, Germany

Correspondence: heike.kalesse-los@uni-leipzig.de

Abstract. Combined continuous long-term ground-based remote-sensing observations with vertically pointing cloud radar and ceilometer are well-suited to identify precipitation evaporation fall streaks (so-called virga). Here we introduce the functionality and workflow of a new open-source tool, the *Virga-Sniffer* which was developed within the frame of RV *Meteor* observations during the ElUcidating the RolE of Cloud–Circulation Coupling in ClimAte (EUREC^{4}A) field experiment in Jan–Feb 2020 in the Tropical Western Atlantic. The *Virga-Sniffer* Python package is highly modular and configurable and can be applied to multilayer cloud situations. In the simplest approach, it detects virga from time-height fields of cloud radar reflectivity and time series of ceilometer cloud base height. In addition, optional parameters like lifting condensation level, a surface rain flag as well as time-height fields of cloud radar mean Doppler velocity can be added to refine virga event identifications. The netcdf-output files consist of Boolean flags of virga- and cloud detection, as well as base- and top heights and depth for the detected clouds and virga. The performance of the *Virga-Sniffer* was assessed by comparing its results to the Cloudnet target classification resulting from using the CloudnetPy processing chain. 88 % of the pixel identified as virga correspond to Cloudnet classifications of precipitation. The remaining 12 % of virga pixel correspond to Cloudnet-classifications of aerosols and insects (about 7 %), cloud droplets (3 %), or clear-sky (about 1 %). Some discrepancies of the virga identification and the Cloudnet target classification can be attributed to applied temporal smoothing. Additionally, it was found that Cloudnet mostly classified "aerosols and insects" at virga edges which points to a misclassification caused by CloudnetPy internal thresholds. For the RV *Meteor* observations during EUREC^{4}A, about 50 % of all detected clouds with bases below the trade inversion were found to produce precipitation that evaporates before reaching the ground. The most important virga-producing clouds were either anvils of convective cells or stratocumulus clouds. 36 % of the detected virga originated from trade wind cumuli. Small virga with depths below 200 m most frequently occurred from shallow clouds with depths below 500 m, while virga depths above 1 km were mainly associated with clouds of larger depths, ranging between 500 and 1000 m. Virga depth showed no strong dependency on column-integrated liquid water path. The presented results substantiate the importance of low-level precipitation evaporation in the lower winter trades. Possible applications of the *Virga-Sniffer* within the frame of EUREC^{4}A include detailed studies of precipitation evaporation with a focus on cold pools or cloud organization, or distinguishing moist processes based on water vapor isotopic observations. However, we envision extended use of the *Virga-Sniffer* for other cloud regimes or scientific foci as well.

1 Introduction

Trade wind cumuli are the dominant cloud type in the subtropical Atlantic. They typically occur in the form of shallow cumulus humilis or deeper cumulus with a cloud base located near the lifting condensation level (LCL) below $1\,\mathrm{km}$. Trade wind cumuli make up about two thirds of the cloud coverage in the subtropical Atlantic. The other third consists of clouds bases above $1\,\mathrm{km}$,

30   mainly stratocumulus, stratus or cloud edges near the trade wind inversion at 2–$3\,\mathrm{km}$ (Nuijens et al., 2014, 2015). Precipitation in these clouds mainly forms at temperatures above freezing point by collision and coalescence among droplets formed on the more numerous and smaller cloud condensation nuclei (Reiche and Lasher-Trapp, 2010). Therefore, precipitation generally occurs as light rain/drizzle from stratocumulus and stratus or as showers from well-developed trade wind cumuli (Austin et al., 1995; Baker, 1993). The drop size distribution (DSD) of precipitation is modified by a variety of microphysical processes like

35   coalescence or break up of drops as they fall through unsaturated air (Xie et al., 2016). However, evaporation is the only warm subcloud microphysical process that changes the overall amount of liquid water and includes a phase change (Tridon et al., 2017). Precipitation underneath a cloud base is often visible as fall streaks. If the precipitation evaporates before reaching the ground, these fall streaks are called virga. Evaporation and the resulting cooling rate of air primarily depend on the DSD of the precipitation and on the relative humidity (RH) of the environment. Large droplets evaporate slower than small droplets; at the

40   same time high RH in the subcloud environment result in slower evaporation, whereas low RH accelerates it (e.g. Xie et al., 2016; Tridon et al., 2017).

     Precipitation evaporation contributes to the moisture- and heat budgets of clouds themselves (Emanuel et al., 1994) but also influences the subcloud environment, e.g. due to the formation of cold pools typically caused by precipitation evaporation underneath convective clouds (Langhans and Romps, 2015). Schlemmer and Hohenegger (2014) also found that cold pools

45   resulting from the evaporation of precipitation lead to an increase of the degree of organization of convection, meaning the aggregation of clouds into larger clusters. The strength of low level precipitation evaporation and the resulting evaporative cooling causes differences in cold pool strength and size, which has an effect on the evolution of the convection (Dawson et al., 2010). This shows that on the one hand precipitation evaporation is important for the organization and regeneration of cloud fields via cold pools, but on the other hand this organization of cloud fields is important for precipitation formation. This

50   close connection results in an impact of precipitation evaporation on the radiation budget, as well as moisture and heat fluxes (Snodgrass et al., 2009). Summarizing, these studies highlight the need to detect precipitation evaporation of convective clouds reliably.

     The numerous research efforts made to further understand trade wind clouds, precipitation formation within them and the connection to cloud microphysics as well as cloud organization culminated in the field campaign for ElUcidating the RolE

55   of Cloud–Circulation Coupling in ClimAte (EUREC[4]A, (Bony et al., 2017; Stevens et al., 2021)). EUREC[4]A was „the most ambitious effort ever to quantify how cloud properties co-vary with their atmospheric and oceanic environment across an enormous (mm to Mm) range of scales“ Stevens et al. (2021). The campaign consisted of about five weeks of measurements in the winter (dry season) trades of the Tropical North Atlantic upstream of Barbados in January and February 2020. It included observations of cloud microphysics, cloud-circulation interactions, air-sea interaction, ocean sub-mesoscale processes, and

60 ocean mesoscale eddies (Stevens et al., 2021). Airborne measurements were carried out by four research airplanes, 2600 radio- and dropsondes and several uncrewed aerial systems. Shipborne measurements were realized by multiple unmanned drifters, five saildrones and four research vessels. In this study, ground-based remote-sensing observations performed onboard the research vessel (RV) *Meteor* operating about $200\,\mathrm{km}$ upwind of Barbados between 12.5 and $14.5\,°\mathrm{N}$ along the $57.25°\,\mathrm{W}$ meridian are utilized to detect and characterize virga.

65 The structure of the manuscript is as follows: The relevant instrumentation and datasets for detection of precipitation and virga including the Cloudnet target classification will be described briefly in Sect. 2. The *Virga-Sniffer* tool developed in this study will be introduced in Sect. 3. To validate the tool, *Virga-Sniffer* results will be compared to the Cloudnet target classification in Sect. 4. This section also presents statistical results of detected virga from clouds below the trade inversion height in context with cloud macrophysical properties for the entire EUREC^{4}A RV *Meteor* observations (18 January to 19 February 70 2020). Sect. 5 comprises a summary, conclusions, and an outlook.

2 Data sets

In the development of the *Virga-Sniffer*, ground-based remote-sensing observations from a Doppler cloud radar and a ceilometer operated onboard RV *Meteor* during EUREC^{4}A for the period from 18 January to 19 February 2020 were utilized. In the following, the used instrumentation and datasets which are publicly available on the EUREC^{4}A AERIS portal (https: 75 //observations.ipsl.fr/aeris/eurec4a/, last access: 12 August 2022), will be described briefly. A summary of instrument specifications is given in Table 1. The Cloudnet processing chain is also briefly described. As additional data, observations from the onboard RV *Meteor* weather station operated by the German Meteorological Service (DWD) that provided continuous observations of standard meteorological parameters such as pressure, temperature, relative humidity, dewpoint temperature, and precipitation were used, e.g. for flagging times when rain was observed at ground and to determine the lifting condensation 80 level (LCL).

2.1 Doppler cloud radar LIMRAD94

The Doppler cloud radar that was installed onboard RV *Meteor* is a bi-static frequency-modulated continuous wave (FMCW) radar-radiometer system of type RPG-FMCW-94-DP operating actively in the W-band ($94\,\mathrm{GHz}$) and containing a passive radiometer channel at $89\,\mathrm{GHz}$ (Küchler et al., 2017). The cloud radar was operated by the Leipzig Institute for Meteorology 85 (LIM) of University of Leipzig, the instrument is named "LIMRAD94" in the following. While it had previously been used for long-term high-resolution cloud-profiling observations on land (Vogl et al., 2022; Schimmel et al., 2022), EUREC^{4}A was the first ship-deployment of LIMRAD94. To avoid sea-spray accumulating on the cloud radar antenna radomes, the radar was placed on the navigation deck of the ship at $15.8\,\mathrm{m}$ above sea level, $4.1\,\mathrm{m}$ in the starboard direction and $11\,\mathrm{m}$ from the centre of the ship towards the stern.

90 The two radar chirp program settings used from 17 to 29 January 2020, and 31 January 2020 onwards, are shown in Table 2. Due to tests and maintenance, no cloud radar data is available for Jan 30, 2020. The vertical range covered by the cloud radar
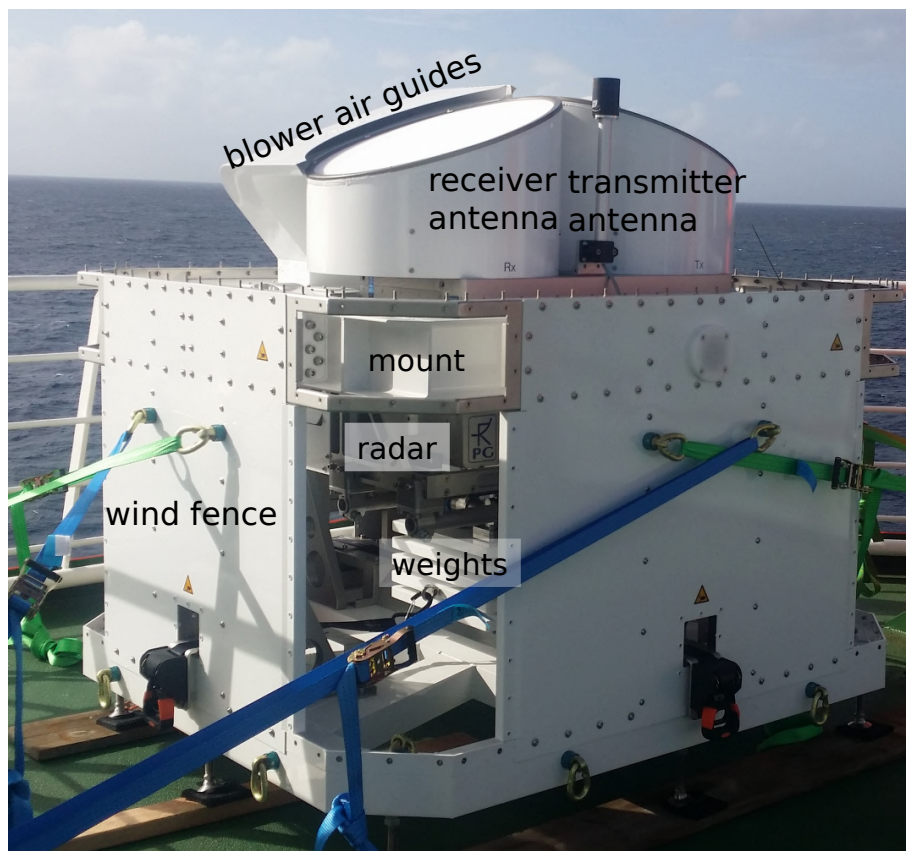
Figure 1. 94 GHz FMCW cloud radar "LIMRAD94" inside the cardanic mount. Specific parts of the radar and the cardanic mount are labeled. Photo taken by H. Kalesse-Los.

observations using the two different chirp table settings was 300–15000 m and 300–13000 m, respectively. Vertical range gate spacing was between 22–42 m, the temporal resolution amounted to 2.9 s and 1.6 s, respectively.

To exclude the effect of horizontal wind on the observed radar Doppler velocities, the radar needs to point to zenith. To
95 assure that, the instrument was operated within a novel two-axle cardanic mount stabilization designed and manufactured by Radiometer Physics GmbH, Meckenheim, Germany which allowed for "free-swinging" of the radar to compensate for ship roll- and pitch angles of up to $\pm 20°$. An illustration of the radar set-up with cardanic mount is given in Figure 1. Continuous attitude angle measurements by radar built-in motion sensors sampling at 0.5 Hz with an accuracy of $0.02°$ showed that observed roll and pitch angles experienced by the radar generally were less than $0.09 \pm 0.49°$ (mean $\pm$ standard deviation). A detailed
100 description of the performance of the radar stabilization platform is beyond the scope of this paper and will be discussed in a separate manuscript.

As a post-processing step to correct for vertical heave of the vessel, a heave correction as described in Acquistapace et al. (2022) was applied to the cloud radar data. Note, that contrarily to Acquistapace et al. (2022), the heave correction was directly

applied to the full Doppler spectrum of the W-band radar, instead of to the mean Doppler velocity. Further radar data processing
105 included signal clutter filtering as well as Doppler spectra dealiasing.

2.2 Ceilometer

From profiles of attenuated backscatter coefficient β_{att} at a wavelength of 1064 nm obtained with a ceilometer type Jenoptik
CHM15kx, cloud bases were determined using the internal ceilometer cloud base detection algorithm. The ceilometer observa-
tions had a range resolution of 15 m and a time resolution of 30 s. It was operated by the Max Planck Institute for Meteorology,
110 Hamburg, Germany. For the CHM179158 ceilometer, deployed onboard RV *Meteor* at 20 m above sea level, the normaliza-
tion factor (so-called TBC value) was 0.496633. In order to obtain β_{att}, an additional factor of 3.2e-12 is needed, resulting
in an overall ceilometer calibration factor of 1.5892256e-12 (personal communication with F. Jansen, MPI for Meteorology,
Hamburg), which is prescribed during Cloudnet processing (see Sect. 2.4) via a metadata dictionary.

2.3 Microwave radiometer LIMHAT

115 Column-integrated values of liquid water path (LWP) and integrated water vapour (IWV) were retrieved from a microwave
radiometer (MWR) type RPG-HATPRO Generation 5 that was placed in the vicinity of the cloud radar on the navigation deck
of the RV *Meteor*. The passive instrument measures brightness temperatures over a range of different frequencies at the centre
and slopes of the atmospheric water vapour absorption line (22.23–31.4 GHz) and the oxygen absorption complex (51.26–
58.0 GHz). To retrieve IWV and LWP from the measured brightness temperatures, statistical algorithms were used by means
120 of a multi-linear regression between modelled brightness temperatures and atmospheric profiles (Löhnert and Crewell, 2003).
The retrieval algorithms are based on a radiosonde dataset gathered in the subtropical Atlantic (Barbados).

2.4 Cloudnet target classification

The Cloudnet processing scheme (Illingworth et al., 2007) combines ground-based remote sensing observations from cloud
radar, backscatter lidar (e.g. ceilometer) and microwave radiometer with additional information from a numerical weather pre-
125 diction model to yield a variety of Cloudnet products, which describe the cloud properties in the vertical column above the
observation site. One of these products is the Cloudnet target classification, which indicates which parts of the atmosphere
above the site contain ice, liquid, aerosol, insects, etc. Here, we are using the Cloudnet target classification classes for consis-
tency checks of the virga detection method.

To obtain the Cloudnet target classification mask, we applied code from the Cloudnetpy package (version 1.33.0, Tukiainen
130 et al., 2020), i.e. a Python package implementing the Cloudnet processing scheme, to the ground-based remote-sensing obser-
vations obtained during EUREC[4]A onboard the RV *Meteor*. With respect to the original Cloudnet software written in Matlab
and C, several updates have been made in the Python version, including e.g. improvements in the detection of the melting
layer, of liquid layers and of insects that still need to be evaluated. Cloudnetpy is an open source project which is being actively

Table 1. Specifications of instruments and measured quantities used in this study.

Data Source	Frequency f / Wavelength λ	Measured / received quantity	Temporal Resolution	Vertical Range	Vertical Resolution
LIMRAD94	$f = 94$ GHz	Spectral power $S_n(v)$			
		Equivalent reflectivity Z_e	2.93 s	300-15000 m	22.4-29.8 m
		Mean Doppler velocity V_m	1.59 s	300-13000 m	22.4-42.1 m
		Spectrum width SW			
LIMHAT	$f = 51.0 - 58.0$ GHz	Brightness temperature	1 s		column integral
		Liquid water path LWP			
Ceilometer	$\lambda = 1064$ nm	Attenuated backscatter coefficient	30 s	15-15000 m	15 m

Table 2. Specifications and program settings for LIMRAD94. Two main chirp tables with slightly different settings were used during the campaign. The upper row denotes the first chirp table operated from 17 to 29 January 2020 18:00 UTC, the second row refers to the second chirp table operated from 31 January 2020 22:28 UTC to 29 February 2020 (here data until 19 February 2020 obtained in the EUREC[4]A region of interest was used.

Attributes	Chirp Sequence 1	Chirp Sequence 2	Chirp Sequence 3
Integration time [s]	1.022	0.947	0.966
	0.563	0.573	0.453
Range interval [m]	300-3600	3600-8000	8000-15000
	300-3000	3000-6200	6200-13000
Range vertical resolution [m]	22.4	25.6	29.8
	22.4	37.7	42.1
Nyquist velocity [m s^{-1}]	6.4	5.2	2.9
	7.3	6.1	4.5
Doppler velocity resolution [m s^{-1}]	0.050	0.081	0.089
	0.057	0.095	0.070
Doppler velocity bins	256	128	64
	256	128	128

Atmospheric
Measurement
Techniques
Discussions
Open Access
EGU

developed by a growing community of users. For these reasons, the Python version of the code was chosen instead of the

135   original (proprietary) Matlab/C implementation of the Cloudnet processing scheme.

For the LIMRAD94 cloud radar, filtering of the data was performed to exclude periods when the chosen radar settings are not supported by Cloudnetpy and would lead to erroneous results. Hourly profiles of pressure, temperature, and relative humidity from the European Centre for Medium-Range Weather Forecast (ECMWF) complemented the input to Cloudnetpy.

3   Methodology - Description of the *Virga-Sniffer*

140   The *Virga-Sniffer* is a profile-based detection scheme for virga events. It is a self-developed Python package (Witthuhn et al., 2022). This package provides a tool for detecting virga from profiles of vertically-pointing cloud radar reflectivity and ceilometer observations of cloud base height (CBH), taking into account multilayer cloud situations. It is highly configurable, modular and therefore usable for different measurement setups. In addition, virga detection can be refined by additionally considering radar mean Doppler velocity, LCL, and surface rain detection.

145   The workflow of the virga detection is separated into three parts, as summarized in Fig. 2:

1. Preprocessing of CBH

2. Precipitation and cloud detection

3. (Optional) Virga detection refinement

3.1   Cloud-base pre-processing

150   The input CBH layer data is pre-processed before it is used for virga and cloud detection. For this processing, modular methods are applied to the CBH input data, which can be individually configured. In total five modules (described below) are available, used settings and thresholds are summarized in Sect. A. Prior to the configurable processing, the CBH data is smoothed, which corresponds to processing module five:

1. *clean & sort*: First, CBH layers with less valid data-points than the given threshold of 5 % are removed (*clean*). Then,
155   for the remaining layers, the mean height of each layer is calculated. The CBH dataset is then re-indexed, by sorting the layers in ascending order by mean height (*sort*).

2. *split*: The CBH dataset is iterated successively layer by layer. For each layer, outliers according to given threshold settings (500 m above and below the current layer mean) are identified and added to new layers created above and below the current layer. This process is re-iterated until no new layers are created.

160   3. *merge*: Merging CBH layer data by successively iterating all layers and comparing lower layers to all layers above them. If the distance of the compared layers is smaller than the given threshold setting (500 m above current layer mean), upper layer data will be re-assigned to the lower layer, or merged by mean value if both layers hold valid data.
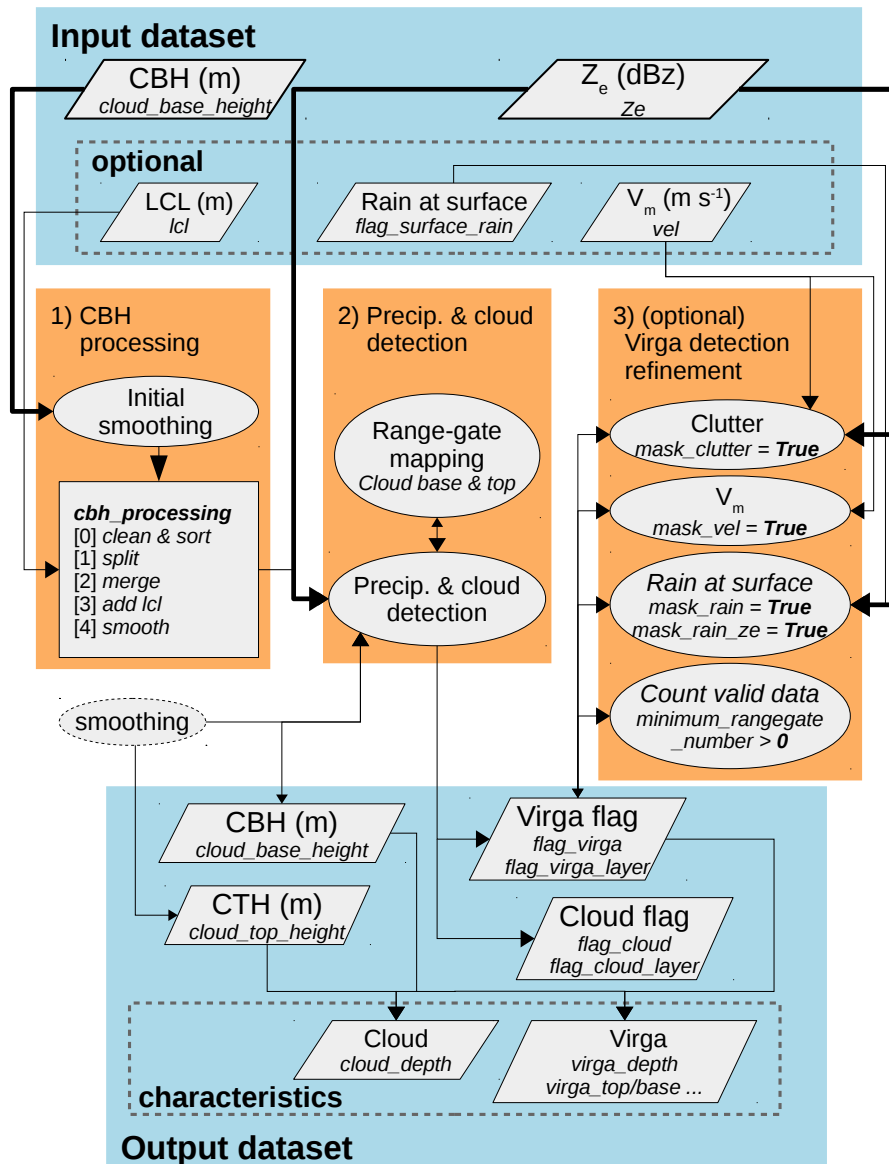
Figure 2. The workflow of the *Virga-Sniffer* virga detection. Datasets are shown as polygons, applied methods as ellipses. The submodule *cbh_processing* is shown as square, listing implemented methods. Z_e and V_m refer to the radar variables reflectivity and mean Doppler velocity, respectively.

4. *add LCL*: If LCL is provided, nan-values of the lowest CBH layer are replaced with the LCL data from the input dataset. The input LCL data is smoothed by applying a running-median filter of a five minutes window size.

165   5. *smooth*: The CBH layer data is smoothed by applying a running-median filter with the window size of one minute.

For the pre-processing of the EUREC^{4}A RV *Meteor* CBH data, two iterations of the combination *split*, *merge*, *add LCL* are considered, followed by an additional smoothing step. The module *clean & sort* is applied in between each step to continuously filter outliers. Note, that here additional data of LCL is required, which is calculated from surface observations of air pressure, temperature and humidity from the meteorological observation station on the RV *Meteor* using the method of Romps (2017),
which is build into the *Virga-Sniffer* package utilities.

As a final step, gaps smaller than one minute in the processed CBH data are filled by linear interpolation to increase the detection coverage, assuming negligible variability of CBH during this time frame. Larger gaps remain, as filling them might lead to non-physical results of CBH and false positive virga detection.

3.2 Precipitation and cloud detection

After the pre-processing of CBH, the radar reflectivity values, specifically the Boolean mask of valid reflectivity values, is used for the initial step of detecting precipitation, clouds and cloud-top heights (CTH). This is done by successively iterating the radar reflectivity mask, starting from each cloud-base in both up- and downward direction. Figure 3 shows a demonstration example for precipitation, virga and cloud detection.

Precipitation is detected at each range-gate of valid radar reflectivity iterating downward from CBH until a gap (nan-value in radar reflectivity) occurs, which is larger than the threshold of $700\,\text{m}$. This threshold is large by choice, to also capture precipitation which can be observed from fall streaks advected to the radar viewing volume by wind shear. At the same time, the threshold is still small enough to mask out any clutter or unidentified clouds close to the surface or a lower cloud layer, respectively.

Similarly, valid radar reflectivity values from the cloud base upward are identified as clouds until a gap larger than the threshold of $150\,\text{m}$ occurs. The CTH value is assigned to the radar range gate value (top of range gate) of the last valid radar reflectivity value below the gap. Note, that the detection of clouds is always limited to the area between cloud base and top, while virga or precipitation cannot be detected in this range.

A special case occurs, when there are no gaps in radar reflectivity between some cloud base layers, which happens when precipitation from a higher cloud falls into a lower cloud. In this case, the intervening cloud layers are excluded. Therefore, the virga or precipitation events are connected and assigned to the highest continuous cloud base and associated cloud.

The detected cloud-top values are smoothed as cloud-base values are smoothed prior to the cloud-base processing utilizing a rolling median filter of a one-minute window size. After this processing step, an index mapping of CTH and CBH values to the upper edge of radar range-gate heights is conducted for further processing. This mapping is used to separate the cloud- and virga-mask into cloud layer components.

Until this point, the identification of clouds and precipitation is solely based on the CBH and radar reflectivity. To actually detect virga instead of precipitation, the information of surface rain is required. Based solely on CBH and radar reflectivity, this is achieved by testing the lowest range-gate reflectivity value against the empirical threshold of $0\,\text{dBz}$. If the radar reflectivity is larger, the precipitation is assumed to reach the surface. These situations are therefore excluded from the virga detection mask.

Virga and cloud detection is sketched in Fig. 3 to highlight special cases and usage of certain thresholds. Special cases are:
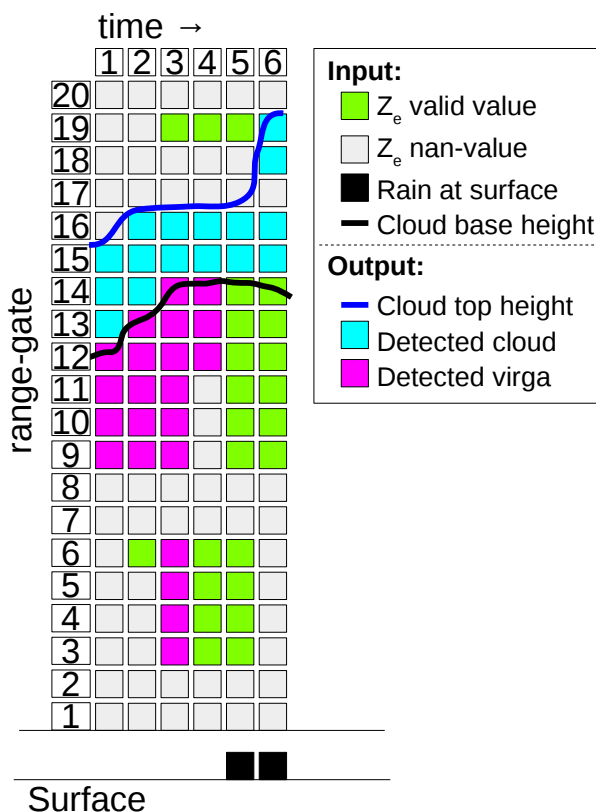
Figure 3. Sketched representation of virga and cloud detection from radar reflectivity Z_e, surface rain flag and cloud base height data.

- *time-step = 2*: The gap (range-gate (rg) 7–8) is smaller than maximum allowed gap for virga to count rg 6 as virga, but rg 6 is filtered since the requirement of minimum virga length of 2 rg is not met.

- *time-step = 3*: The gap (rg 7–8) is smaller than the threshold, therefore rg 3–6 are counted as virga.

- *time-step = 4*: The gap (rg 7–11) is larger than the threshold, therefore rg 3–6 are not counted as virga. In addition, the gap (rg 17–18) is larger than the maximum allowed gap for clouds, therefore rg 19 is not counted as cloud.

- *time = 5*: Rain is observed at the surface (either by the additional data of surface rain flag, or by exceeding the radar reflectivity threshold in the lowest rg), therefore no virga is assigned in this profile.

- *time-step = 6*: Same as *time-step = 5*. In addition, the gap (rg 17) is smaller than the maximum allowed gap for clouds, therefore rg 18–19 are counted as cloud.

10

Atmospheric
Measurement
Techniques
Discussions
Open Access
EGU

3.3 Virga mask refinement

210 As a first step of virga mask refinement, virga events of each profile spanning less than two range-gates are excluded to remove false positive detection due to clutter (see Fig. 3, *time-step* = 2). In addition, clouds and virga detection solely based on radar reflectivity and CBH is refined by using additional data of mean Doppler velocity and surface rain flag.

To mask rain events from the virga detection, the *Virga-Sniffer* provides two methods. The first is based on the radar reflectivity value at the lowest range-gate (here: 300 m) which is compared to a threshold of 0 dBz as described above. If additional
215 data of surface rain detection is included, this can be incorporated to refine the masking of rain events. In this study, surface rain detection is acquired from the precipitation sensor of the ship's meteorological station.

By using the radar mean Doppler velocity, two additional refinements of the virga mask can be enabled. Firstly, to restrict virga to only falling hydrometeors each data-point is checked against a threshold of $0 \, \mathrm{m \, s^{-1}}$. Data-points with positive values of mean Doppler velocity (upward) are omitted from the virga mask (*mask_vel*, see Fig. A1). Secondly, to mask clutter events,
220 the virga mask is restricted to data-points fulfilling the following dependency:

$$V_m > -m * (Z_e/60(\mathrm{dBz})) + c \tag{1}$$

where V_m and Z_e denotes the input mean Doppler velocity $(\mathrm{m \, s^{-1}})$ and radar reflectivity factor (dBz), respectively. For convenience, Z_e is scaled by 60 dBz, as -60 dBz is the minimum valid reflectivity value of LIMRAD94 (for the used radar chirp settings, see Table 2). Slope and intercept of the threshold line are denoted as m $(\mathrm{m \, s^{-1}})$ and c $(\mathrm{m \, s^{-1}})$, respectively. A
225 data point is considered virga only if Eq. 1 is fulfilled. With default configuration (m = 4 and c = -8) unusual combinations of low Z_e and V_m are filtered (*mask_clutter*, see Fig. A1).

3.4 *Virga-Sniffer* output examples

Example cases of virga detection from RV *Meteor* observations during EUREC[4]A for which all outlined *Virga-Sniffer* workflow steps were applied, are shown in Fig. 4. The case study examples illustrate the applicability of the *Virga-Sniffer* to different
230 cloud scenarios such as stratocumulus with virga and a precipitation system (type flower, following the cloud organization pattern naming convention of Stevens et al. (2019)) with virga (Fig. 4 (a) and (b)), mid-level-clouds such as virga-producing altocumulus (Fig. 4 (c) and (d)) and virga originating from trade-wind cumuli in different development stages (Fig. 4(a) and (b) as well as (e) and (f)) including multi-layer cloud situations.

For easy usability of the *Virga-Sniffer* results, the virga and cloud detection masks are stored in an output dataset as boolean
235 flags with the same dimensions (time, height) as the radar reflectivity input data. In addition, the processed cloud- and virga base- and top heights are stored, as well as some basic characteristics such as cloud depth and virga depth for each profile.

3.5 Limitations

The virga detection is strongly tuned and manually evaluated for best performance of the EUREC[4]A RV *Meteor* dataset (see Sect. 2) and relies on threshold based tests which might not work in other measurement conditions or different instrumental
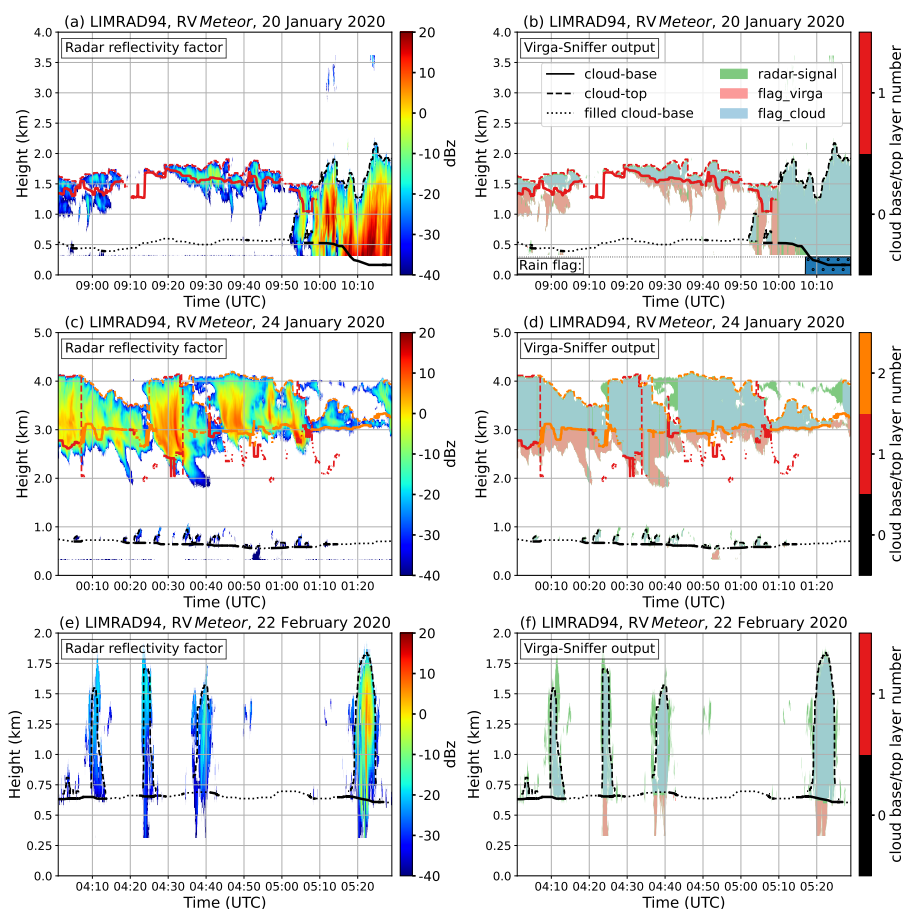
Figure 4. *Virga-Sniffer* output for different cloud situations during EUREC[4]A based on RV *Meteor* observations. The colorbar on the right side panels denote the maximumd number of cloud layers detected during the case study days (count starts at zero for the lowest layer). Panels (a) and (b) show stratocumulus with virga and a precipitation system, panels (c) and (d) altocumulus with virga, and panels (e) and (f) trade wind cumuli with virga.

240   setups. However, the *Virga-Sniffer* was tested with good results without threshold adjustments for a similar dataset measured on
the RV *Maria S. Merian* at EUREC[4]A (Acquistapace et al., 2021). The RV *Maria S. Merian* was operating closer to the Inner
Tropical Convergence Zone (ITCZ) and thus observed more precipitation events. The measurement setup included the same
FMCW-94 GHz cloud radar and cloud base detection from a combination of ceilometer and radar products. Results using the
RV *Merian* data set are not shown in this paper. The virga detection based on both the RV *Meteor* and RV *Maria S. Merian* data

245   sets runs stable without issues. Nevertheless, major caveats using this version of the *Virga-Sniffer* are outlined in this section.

Virga events are associated with a certain CBH. Precipitation below a CBH layer, which does not reach the surface, is considered virga. In case of a non-continuous radar signal (see Figure 5 at around 03:45 UTC) the virga associated with the cloud-base is detected far below the CBH if the gaps are smaller than the maximum allowed virga gap of 700 m. When calculating virga depths using output values of virga-base and virga-top heights, the maximum geometrical extent is calculated. For volumetric

250   characteristics (e.g., LWP) the output variable *virga_depth* should be used, as this value is calculated by excluding these gaps. Anyway, this caveat can be circumvented by not ignoring gaps in virga which can be achieved by setting the maximum allowed virga gap to zero. Doing this would however mean to cut virga events in strongly-tilted fall streaks or those that are slightly disconnected from the observed cloud base. A second issue might arise from this behaviour, as virga detected close to lower layer clouds could as well be undetected clouds. Therefore, refinement of the virga mask using the radar mean Doppler velocity

255   is highly recommended.

If clouds are present in multiple levels, virga detection is challenging, as only the cloud-base is known a priori and the vertical extent of the precipitating cloud is not. The *Virga-Sniffer* includes a cloud- and cloud-top detection which is heavily sensitive to the threshold of maximum allowed gaps of reflectivity values in single profiles for cloud detection. This raises two issues if upper layer clouds are present. First, the maximum allowed gap is too small: Due to uncertainties in observational

260   CBH or radar reflectivity data, misalignment of both data or coarse resolution of radar range-gates, ceilometer detected cloud bases might not connect directly to a valid radar signal. Assume, the CBH value is below the first range-gate with valid radar signal and the signal gap is larger than the maximum allowed gap (as it is the case in Fig. 5 at around 05:00 UTC), the cloud will not be detected and no cloud-top will be assigned. In turn, these range-gates, which are not marked as cloud due to that, will be potentially marked as virga if there would be a higher level cloud with precipitation (this is not the case in Fig. 5).

265   Second, the maximum allowed gap between range-gates with valid radar signal is too large: In this case, clouds will expand over the precipitation from a potential upper layer cloud when they are close to lower layer cloud top height (not the case in Fig. 5).

The data points of radar reflectivity might connect through multiple layers of clouds defined by the ceilometer observed CBH. This is the case for example in Fig. 5 at around 05:00 and 05:45 UTC. During processing with the *Virga-Sniffer*, these cases are

270   assumed to be connected and lower layer CBH values are not evaluated. However, this might result in sudden jumps of virga extent, if gaps in upper layers of cloud-base height occur. These gaps might occur when the ceilometer beam is attenuated by the lower level cloud to a large extent. Gaps in ceilometer data can be filled by increasing the layer filling threshold to increase the coverage of upper layer clouds, but might result in false positive detection. Nevertheless, it is challenging to define
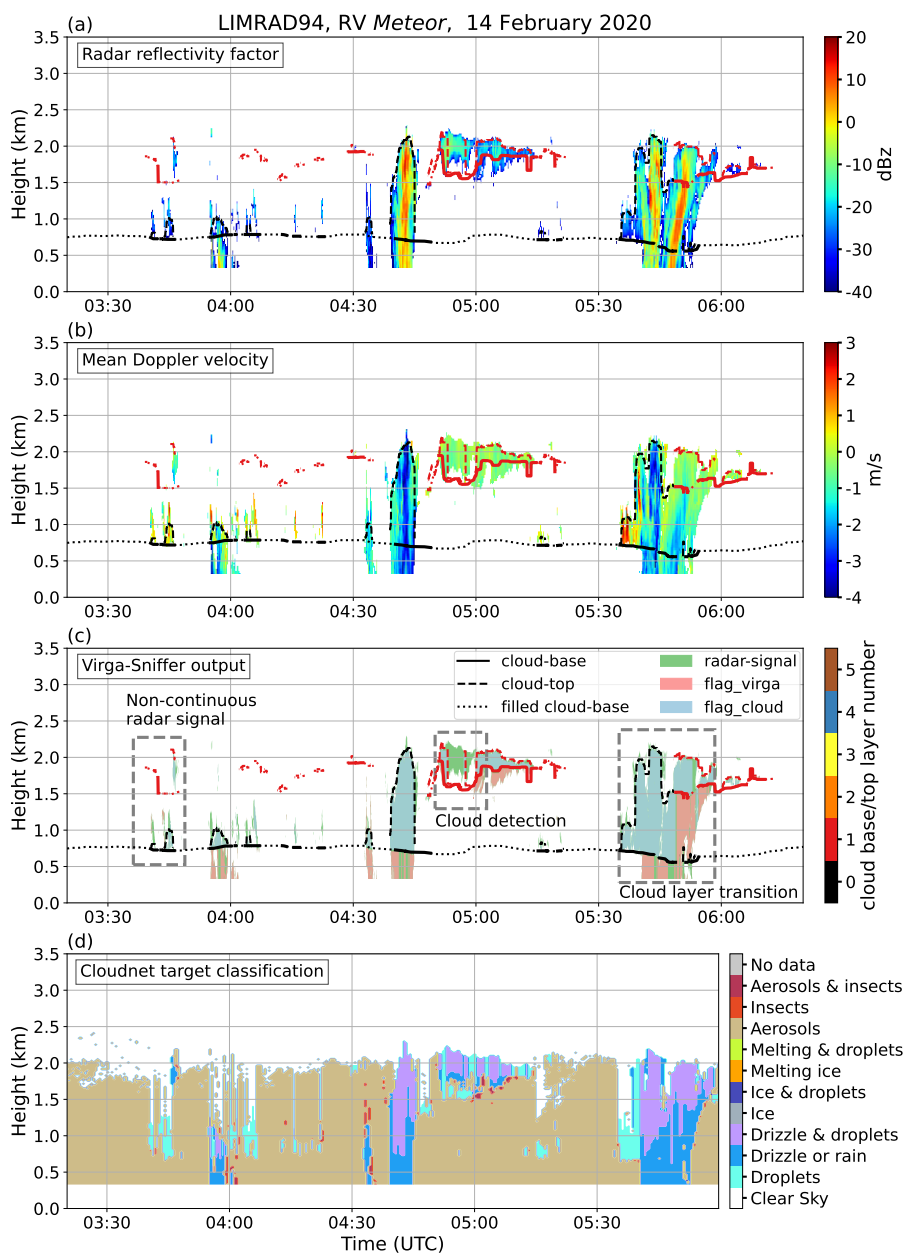
Figure 5. (a) LIMRAD94 reflectivity factor, (b) mean Doppler velocity, (c) *Virga-Sniffer* output and (d) Cloudnet target classification for, 14 February 2020 as observed from RV *Meteor*. The *Virga-Sniffer* output is marked (dashed boxes) to reveal some caveats which include non-continuous radar signals (03:45 UTC); cloud detection (05:00 UTC); multi layer cloud transition (05:45 UTC). The colour bar denotes the number of cloud layers detected on that day (count starts at zero for the lowest layer).

cloud-bases in precipitating clouds, especially if multiple layers of clouds cannot easily be disentangled from the observations.
This situation is likely the source of most false positive virga detections.

4 *Virga-Sniffer* results from RV *Meteor* observations during EUREC[4]A

4.1 Comparison to Cloudnet target classification

In order to assess the credibility of the *Virga-Sniffer*, a comparison to the Cloudnet target classification is made for the
RV *Meteor* observations during EUREC[4]A. Fig. 6 (inner ring) shows the relative frequency of occurrence of the Cloudnet
target classification within virga identified by the *Virga-Sniffer*. The outer ring gives the summarized portion of grouped target
classification such as liquid only, ice-containing, as well as aerosols and insects. Around 61 % of the hydrometeors within the
detected virga are classified by Cloudnet as liquid only, summarizing droplets, drizzle or rain, and the target class drizzle and
droplets. Among these targets, only a small fraction (less than 3 %) corresponds to droplets, meaning the *Virga-Sniffer* performs
well in detecting liquid precipitation. Around 31 % of the pixel identified as virga are among the ice-containing Cloudnet target
classes comprised of ice, ice and droplets, melting ice or melting ice and droplets. In Cloudnet, ice as well as ice and droplets
refer to falling hydrometeors, they make up roughly 30 % of the pixel identified as virga. It can thus be concluded, that the
Virga-Sniffer also performs well in detecting ice precipitation. A small fraction of virga-pixel (1 %) are classified as clear
sky by Cloudnet. This can be attributed to smoothing at precipitation edges in the *Virga-Sniffer* algorithm. About 7 % of the
virga-pixel are Cloudnet-classified as aerosols and insects. As illustrated in the height-resolved overview of the frequency of
occurrence of Cloudnet target classification results within virga in Figure 7, aerosols and insects detected within virga mostly
occurred within the lowermost 2 km and at virga edges (see Fig. 5 panel (d)). This unexpected Cloudnet insect classification
near virga edges is likely caused by strong evaporation leading to radar reflectivity values falling below a threshold value which
will be investigated by us in the near future. Figure 7 also shows that the liquid-only group of Cloudnet targets occurs mostly
below 3 km, while the ice-containing class was mostly detected above 5 km. The separation of the Cloudnet liquid and ice
classes is thus according to the mean freezing level at 4.8 km determined from radiosonde data. The majority of ice-containing
targets between 4 km and 10 km were observed between 14 February and 16 February 2020. Those days featured continuous
and deep cirrus stratus and alto stratus.

4.2 Virga Properties

The statistics in Table 3 and the subsequent plots were created using output of the *Virga-Sniffer*. The results show the importance
of precipitation evaporation in the winter trades of the tropical Western Atlantic. In the following analysis, only clouds with
bases below 4 km, i.e. below the trade inversion height (TIH) are considered. Such clouds were the focus of EUREC[4]A. The
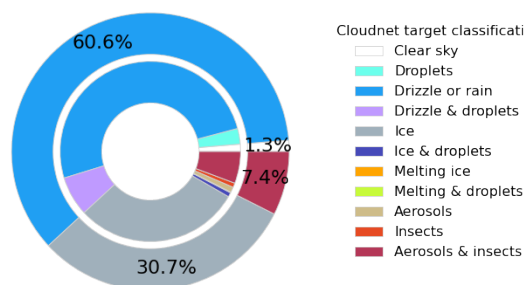relation of virga depth to cloud macrophysical properties, cloud base height and cloud depth is analysed.

Figure 6. Relative frequency of occurrence of the Cloudnet target classification results within virga identified by the *Virga-Sniffer*. The inner ring displays the percentage of the individual Cloudnet target classifications, whereas the outer ring shows the portion of grouped Cloudnet target classes for liquid-only, ice-containing, as well as aerosols and insects.
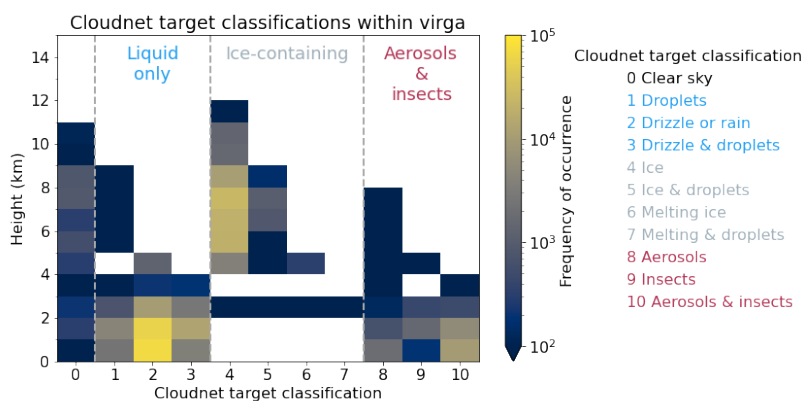

Figure 7. Height-resolved frequency of occurrence of the Cloudnet target classification results within virga identified by the *Virga-Sniffer*. The target classes are grouped into three combined target classes: liquid-only, ice-containing, and aerosols and insects.

4.2.1 Virga statistics

About 75% of all clouds observed on RV *Meteor* during EUREC[4]A had a cloud base below $4\,\mathrm{km}$ i.e. below the TIH. Of these 75%, 60% produced precipitation that was either detected as virga by the *Virga-Sniffer* or as rain reaching the ground by the WS100-UMB surface rain sensor. These 60% of precipitating clouds can be subdivided into about 51% that produced virga and around 9% that produced rain reaching the rain sensor onboard the RV *Meteor*. Of all clouds with bases below the trade inversion, 49% were trade wind cumuli (CBH below $1\,\mathrm{km}$). Approximately 51% of the trade wind cumuli produced precipitation, but less than 12% of all trade wind cumuli produced precipitation that was detected by the DWD rain sensor. The remaining 39% were cumuli that produced virga. With respect to all detected virga from clouds with bases below TIH,

16

Table 3. Precipitation and virga statistics. Precipitation-producing clouds are defined as clouds that either produce virga or rain that reaches the ground. Clouds with ceilometer-detected cloud base below 1 km are classified as trade wind cumuli and considered individually.

Fraction of clouds with cloud base below 4 km:	75.4 %
Precipitation producing clouds:	60.0 %
Raining clouds (rain reaches surface):	8.6 %
Clouds with virga:	51.4 %
Fraction of trade wind cumuli:	49.1 %
Fraction of virga originating from trade wind cumuli:	37.4 %
Trade wind cumuli producing precipitation:	50.8 %
Trade wind cumuli with rain reaching surface:	11.6 %
Trade wind cumuli with virga:	39.2 %

trade wind cumuli only made up about 37 %, the remaining 63 % of virga originated from clouds with bases between 1 km and TIH.

4.2.2 Virga depth and cloud base height

Figure 8 shows a 2D histogram of virga depth vs. cloud base height. The pronounced line extending from lower left to upper
315 right of the plot is caused by virga reaching the lowest radar range gate at 300 m, since radar-based detected virga depth cannot be larger than CBH minus the lowest radar range gate height. A large number of virga with varying depths originate from trade wind cumuli which have cloud bases at the LCL between 600 and 800 m. These virga reach the lowest radar range gate most frequently and evaporate near the surface. Clouds with bases around 1.5 km and 2.5 km most often produce shallow virga with depths up to 200 m. In these heights, mostly stratocumulus are present, reaching up to the base of the trade inversion. From
320 these mostly shallow clouds, shallow virga originate that evaporate before reaching the lowest radar range gate. However, occasionally virga from these clouds can also reach the lowest radar range gate. This underlines the importance of precipitation evaporation especially in the lowest 300 m of the mostly well-mixed subcloud layer.

4.2.3 Virga depth and cloud depth

Figure 9 illustrates the relation of cloud depth and virga depth. Figure 8 panel (a) shows this relation for clouds with their base
325 below 1 km, respectively the trade wind cumuli. No clear dependency between virga depth and cloud depth can be seen. Large cloud depths combined with small virga depths are likely stronger convective cells (cumulus congestus) with a CBH near the LCL and higher vertical extent. The maximum virga depth the *Virga-Sniffer* can determine is confined by the distance between cloud base and lowest radar range gate. Thus, virga depth values in (a) are restricted to a few hundred meters. Figure 9 (b) includes only clouds with their base above 1 km and below the TIH. Those are mostly stratocumulus, cloud edges and anvils of
330 convective cells spreading under the trade inversion. Virga depths smaller than 0.3 km often occur from shallow stratocumulus
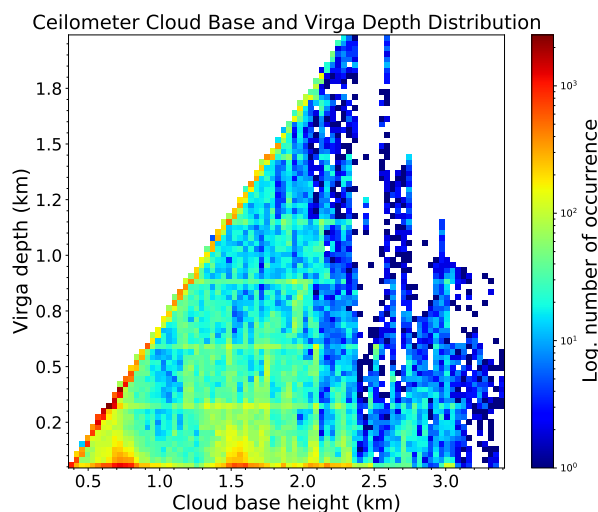
Figure 8. 2D histogram of cloud base height and virga depth. The colorbar is logarithmic.

with depths below 0.5 km. For cloud depths between 0.5 and 1 km, the occurrence of virga depths between 0.3 and 1 km is rather evenly distributed. This shows that, inside these boundaries, virga depth is not very dependent on cloud depth. This is also valid for cloud depths between 1 and 1.5 km and virga depths up to 1 km, although these combinations are detected less frequently. Virga depths above 1 km are most frequently produced by clouds with depths between 0.5 and 1.5 m. Those clouds

335 are mainly thick stratocumulus and anvils below the trade inversion, with a cloud base that is high enough to produce deep virga. In a further analysis, the relation of virga depths and liquid water path (LWP) was studied. It is not presented, since no strong dependency of virga depth on column-integrated liquid water path was found.

5 Summary, conclusions and outlook

Based on the importance to identify precipitation evaporation reliably, we developed the so-called *Virga-Sniffer*, a new freely-
340 available Python package (Witthuhn et al., 2022). It uses profile-by-profile ground-based remote-sensing observations of ceilometers for cloud-base height detection and vertically-pointing Doppler cloud radar to identify clouds and (evaporating) precipitation, and is applicable to multilayer cloud situations. The *Virga-Sniffer* tool is modular and highly configurable, and can thus be applied to different measurement setups.

In this manuscript, the functionality and workflow of the *Virga-Sniffer* tool is explained in detail. It is noteworthy, that while
345 for the most basic approach, only time-height fields of cloud radar reflectivity and time series of cloud base height (CBH) are required, the modular approach of the *Virga-Sniffer* allows for including other optional parameters such as LCL, a surface rain flag, and time-height fields of cloud radar mean Doppler velocity allowing for refinements of the virga event identifications. The *Virga-Sniffer* output does not only contain the actual Boolean flags of virga- and cloud detections in the same time-height

Atmospheric
Measurement
Techniques
Discussions
Open Access
EGU
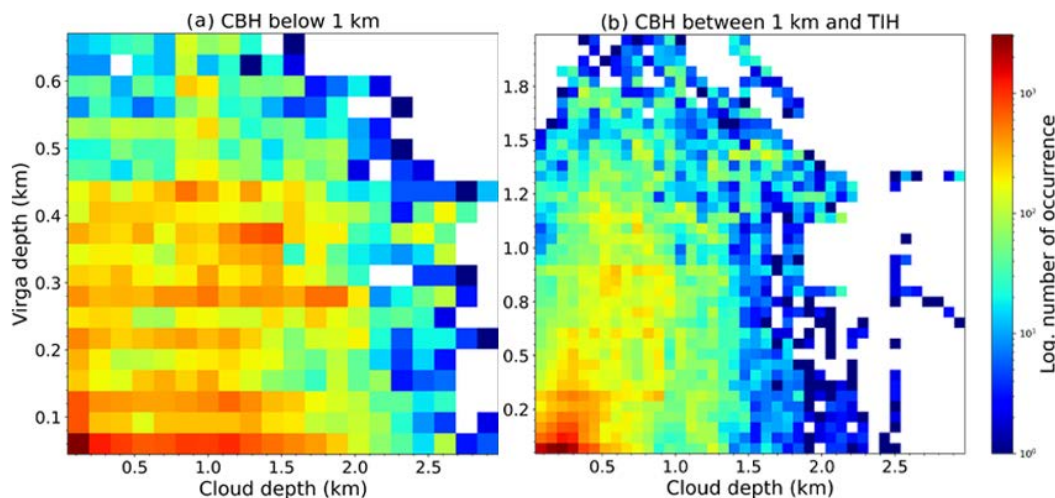
Figure 9. 2D Histograms of cloud depth and virga depth. The colorbar is logarithmic. In panel (a) cloud depths and virga depths for clouds with a base below 1 km are shown. Panel (b) shows the same but for clouds with their base between 1 km and the trade inversion height (TIH).

grid as the radar input data, but it also provides a number of the virga- and cloud properties, including base- and top heights

350 as well as depth. Limitations of the *Virga-Sniffer* are also described. We would like to point out that the virga detection with the *Virga-Sniffer* was developed and optimized for the RV *Meteor* dataset obtained during EUREC[4]A. Its performance was, however, also successfully evaluated for EUREC[4]A-observations of the RV *Maria S. Merian* without modifications of the thresholds. RV *Maria S. Merian* observations were obtained closer to the ITCZ, where more frequent precipitations events were observed. For different instrument setups, cloud types or climate zones, threshold modifications by the *Virga-Sniffer* user

355 are needed to optimize the results.

To evaluate the *Virga-Sniffer*, we compared the detected virga events to the Cloudnet target classifications. Summarizing, within all pixel classified as virga by the *Virga-Sniffer*, 88 % were classified by Cloudnet as precipitation (58 % liquid-phase, 30 % ice-phase). The remaining 12 % are either Cloudnet-classified as aerosols and insects (about 7 %), cloud droplets (3 %), or clear-sky (roughly 1 %). We conclude that the performance of the *Virga-Sniffer* compared to the Cloudnet target classification

360 is good. Some discrepancies are expected due to smoothing at precipitation edges as well as ceilometer CBH-smoothing as part of the pre-processing of the *Virga-Sniffer*. The Cloudnet-classification "aerosols and insects" mostly occurred at virga edges and is likely related to Cloudnet-thresholds for target classifications, which we will explore further.

As application, the *Virga-Sniffer* tool was used for virga identification for the entire RV *Meteor* dataset gathered within the frame of EUREC[4]A from 18 January to 19 February 2020.

365 Statistical results showed that 75 % of the observed clouds had bases below 4 km; 49 % of them were trade wind cumuli with a cloud base below 1 km.

For the RV *Meteor* dataset, 51 % of all clouds below 4 km produced precipitation that evaporated before reaching the ground. This marks the importance of precipitation evaporation in the lower winter trade wind zone. W.r.t. all detected virga from cloud bases below the freezing level, virga from trade wind cumuli make up about 37 %. Trade wind cumuli were found to produce

370   virga of varying depths, but a large fraction of these virga tend to reach the lowest radar range gate in 300 m. This means the precipitation evaporates between 300 m and ground level and therefore has a strong contribution to near-surface evaporation. Clouds with bases between 1 km and 4 km, which are either cloud edges of convective cells or stratocumulus forming below the trade inversion, were identified as important virga producers. Stratocumulus and stratus with their base around 1.5 km and 2.5 km frequently produce either virga with small depths up to 200 m or virga reaching the lowest radar range gate. This means

375   their virga can reach depths of over 1.5 km and shows that they also contribute to low level evaporation.

We would like to finish this study with highlighting for which kinds of studies the *Virga-Sniffer* might for example be used for in the future. A straightforward application is to use the *Virga-Sniffer* for identifying virga and determining macrophysical properties such as virga depth in relation to cloud base height and cloud depth as they are a pre-requisite for detailed evaporation studies as e.g. done by Xie et al. (2016); Tridon et al. (2017).

380   Other possible applications of the *Virga-Sniffer* include enhancing studies of precipitation evaporation in the context of cold pools and cloud organization within the frame of EUREC[4]A as e.g. done by Vogel et al. (2021); Touzé-Peiffer et al. (2022). Additionally, studying precipitation and virga characteristics coupled with water vapour isotopic measurements which was also a focus of EUREC[4]A (Bailey et al., 2022) can help to discern the balance of moist processes which set the humidity profiles. While the *Virga-Sniffer* was developed within the context of EUREC[4]A and the shown results here focus on warm clouds,

385   the tool is highly modular and configurable and thus applicable to study precipitation evaporation or sublimation originating from other cloud types such as ice and mixed-phase-clouds and can be used in other geographic settings such as orographic terrain or the Arctic. As a near-future goal, we would like to apply it to the long-term BCO remote-sensing dataset to contrast precipitation evaporation in the dry and wet season. Additionally, an integration of the *Virga-Sniffer* CBH pre-processing into the open-source project Cloudnetpy is conceivable in order to achieve an improvement of the CBH in situations with multi-layer

390   cloud cover.

Appendix A: *Virga-Sniffer* recommended configuration

The *Virga-Sniffer* utilizes a variety of flags and thresholds to detect virga from the given input data. The configuration can be set via a configuration dictionary, which will be merged with the default values. In the following all default values of configuration flags, thresholds and settings are summarized. A full description can be found in the documentation (https:

395   //virga-sniffer.readthedocs.io, last access 19 August 2022) (Witthuhn et al., 2022).

A1   Flags

Flags are boolean values which control certain functionality of the *Virga-Sniffer*:

Atmospheric
Measurement
Techniques
Discussions

Open Access

EGU

– *require_cbh* = True: The detected virga always have to be attributed to a cloud-base height (CBH) value. This prevents false positive detection of virga which actually would be a cloud in case of data-gaps in the ceilometer CBH data.

400   – *mask_vel* = True: The virga detection is refined by filtering data with mean Doppler velocity values larger than *vel_thres* threshold.

– *mask_clutter* = True: The virga detection is refined by filtering data which is probably clutter based on Eq. 1.

– *mask_rain* = True: This configuration suses the ancillary data of the *flag_surface_rain* variable from the input dataset. Virga is considered only, if no rain is observed at the surface. This is applied to the lowest present cloud layer at any
405   given time.

– *mask_rain_ze*: Similar to *mask_rain*, but instead of using *flag_surface_rain* from the input dataset, the radar reflectivity at the lowest range-gate is tested against the *ze_thres* threshold in order to estimate if precipitation will reach the surface.

A2   Thresholds

Virga detection specific thresholds:

410   – *minimum_rangegate_number* = 2: In case of non-continuous radar signal in a profile, isolated contiguous range-gates with valid radar signal are used only if the number of range-gates is greater than this threshold.

– *ze_max_gap* = 150 m: Assigns the maximum allowed gap for cloud detection.

– *virga_max_gap* = 700 m: Assigns the maximum allowed gap for virga and precipitation detection.

– *vel_thres* = $0\,\mathrm{m\,s^{-1}}$: Threshold for the virga detection refinement based on mean Doppler velocity.

415   – *ze_thres* = 0 dBz: If the value of radar reflectivity of the lowest range is larger than *ze_thres*, precipitation is assumed to reach the ground and not considered as virga in the lowest cloud layer.

– *clutter_m* = $4\,\mathrm{m\,s^{-1}}$: Slope of the linear masking dependency (see Eq. 1).

– *clutter_c* = $-8\,\mathrm{m\,s^{-1}}$: Intercept of the linear masking dependency (see Eq. 1).

Cloud-base preprocessing specific thresholds:

420   – *cbh_smooth_window* = 60 s: Size of the window for the median-filter smoothing of cloud-base height and cloud-top values.

– *lcl_smooth_window* = 300 s: Size of the window for the median-filter smoothing of the lifting condensation level data.

– *cbh_layer_thres* = 500 m: Threshold used for splitting cloud base layers during the preprocessing.

– *cbh_clean_thres* = 0.05: Threshold used for cleaning cloud base layers during the preprocessing.

21

Atmospheric
Measurement
Techniques
Open Access
Discussions
EGU
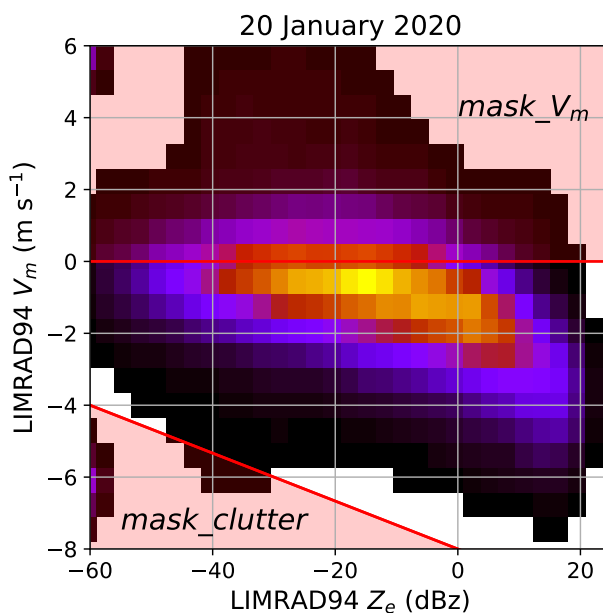
Figure A1. Heatmap of the mean Doppler velocity V_m and radar reflectivity Z_e during EUREC[4]A from the RV *Meteor* on 20 January 2020. Demonstration of masking based on V_m data. Data-points from red hatched regions are not considered as virga. The velocity mask (*mask_V_m*) restricts virga events to falling hydrometeors. The clutter mask (*mask_clutter*) removes non-physical values of high negative V_m while low radar reflectivity factors are observed, which is probably clutter from the radar observation.

425   – *cbh_fill_limit* = 60 s: Defines the maximum gap within cloud layers to be filled by interpolation method cbh_fill_method (see preprocessing).

A3   Special configuration

Apart from thresholds, the cloud-base preprocessing is controlled by specialized configuration:

     – *cbh_fill_method* = slinear: This defines the method of filling cloud-base gaps smaller than *cbh_fill_limit*.

430   – *cbh_processing* = [1, 0, 2, 0, 3, 1, 0, 2, 0, 3, 4]: This list defines the methods applied for preprocessing (see Fig. 2).

Competing interests. The authors declare that they have no competing interests.

References

Acquistapace, C., Schween, J. H., Risse, N., Haseneder-Lind, R., Klocke, D., Röttenbacher, J., Kalesse-Los, H., Coulter, R. L., Bormet, S. M., Myagkov, A., and Rose, T.: Liquid water path and Doppler radar moments observations from the 94 GHz FMCW-band radar deployed on R/V Maria S. Merian during EUREC4A campaign - V2, https://doi.org/10.25326/235, medium: NetCDF Type: dataset, 2021.

465 Acquistapace, C., Coulter, R., Crewell, S., Garcia-Benadi, A., Gierens, R., Labbri, G., Myagkov, A., Risse, N., and Schween, J. H.: EUREC[4]A's *Maria S. Merian* ship-based cloud and micro rain radar observations of clouds and precipitation, Earth System Science Data, 14, 33–55, https://doi.org/10.5194/essd-14-33-2022, 2022.

Austin, P., Wang, Y., Pincus, R., Kujala, V., et al.: Precipitation in stratocumulus clouds: Observational and modeling results, Journal of the atmospheric sciences, 52, 2329–2352, 1995.

470 Bailey, A., Aemisegger, F., Villiger, L., Los, S. A., Reverdin, G., Quiñones Meléndez, E., Acquistapace, C., Baranowski, D. B., Böck, T., Bony, S., Bordsdorff, T., Coffman, D., de Szoeke, S. P., Diekmann, C. J., Dütsch, M., Ertl, B., Galewsky, J., Henze, D., Makuch, P., Noone, D., Quinn, P. K., Rösch, M., Schneider, A., Schneider, M., Speich, S., Stevens, B., and Thompson, E.: Isotopic measurements in water vapor, precipitation, and seawater during EUREC[4]A, Earth System Science Data Discussions, 2022, 1–40, https://doi.org/10.5194/essd-2022-3, 2022.

475 Baker, M.: Trade cumulus observations, in: The Representation of Cumulus Convection in Numerical Models, pp. 29–37, Springer, 1993.

Bony, S., Stevens, B., Ament, F., Bigorre, S., Chazette, P., Crewell, S., Delanoë, J., Emanuel, K., Farrell, D., Flamant, C., Gross, S., Hirsch, L., Karstensen, J., Mayer, B., Nuijens, L., Ruppert, J. H., Sandu, I., Siebesma, P., Speich, S., Szczap, F., Totems, J., Vogel, R., Wendisch, M., and Wirth, M.: EUREC4A: A Field Campaign to Elucidate the Couplings Between Clouds, Convection and Circulation, Surveys in Geophysics, 38, 1529–1568, https://doi.org/10.1007/s10712-017-9428-0, 2017.

480 Bühl, J., Radenz, M., Schimmel, W., Vogl, T., Röttenbacher, J., and Lochmann, M.: pyLARDA v3.2, https://doi.org/10.5281/ZENODO.4721311, 2021.

Dawson, D. T., Xue, M., Milbrandt, J. A., and Yau, M.: Comparison of evaporation and cold pool development between single-moment and multimoment bulk microphysics schemes in idealized simulations of tornadic thunderstorms, Monthly Weather Review, 138, 1152–1171, 2010.

485 Emanuel, K. A., David Neelin, J., and Bretherton, C. S.: On large-scale circulations in convecting atmospheres, Quarterly Journal of the Royal Meteorological Society, 120, 1111–1143, 1994.

Illingworth, A. J., Hogan, R. J., O'Connor, E., Bouniol, D., Brooks, M. E., Delanoé, J., Donovan, D. P., Eastment, J. D., Gaussiat, N., Goddard, J. W. F., Haeffelin, M., Baltink, H. K., Krasnov, O. A., Pelon, J., Piriou, J.-M., Protat, A., Russchenberg, H. W. J., Seifert, A., Tompkins, A. M., van Zadelhoff, G.-J., Vinit, F., Willén, U., Wilson, D. R., and Wrench, C. L.: Cloudnet: Continuous Evaluation of Cloud Profiles in
490 Seven Operational Models Using Ground-Based Observations, B. Am. Meteorol. Soc., 88, 883–898, https://doi.org/10.1175/BAMS-88-6-883, 2007.

Jansen, F.: Ceilometer Measurements RV Meteor, EUREC4A, https://doi.org/10.25326/53, medium: NetCDF,ASCII Type: dataset, 2020.

Kalesse-Los, H., Röttenbacher, J., Schäfer, M., and Emmanouilidis, A.: Microwave Radiometer Measurements RV Meteor, EUREC4A, https://doi.org/10.25326/77, medium: NetCDF Type: dataset, 2020.

495 Kalesse-Los, H., Röttenbacher, J., and Schäfer, M.: W-Band Radar Measurements RV Meteor, EUREC4A, https://doi.org/10.25326/164, medium: NetCDF Version Number: 1.0 Type: dataset, 2021.

Küchler, N., Kneifel, S., Löhnert, U., Kollias, P., Czekala, H., and Rose, T.: A W-Band Radar–Radiometer System for Accurate and Continuous Monitoring of Clouds and Precipitation, Journal of Atmospheric and Oceanic Technology, 34, 2375–2392, https://doi.org/10.1175/jtech-d-17-0019.1, 2017.

500 Langhans, W. and Romps, D. M.: The origin of water vapor rings in tropical oceanic cold pools, Geophysical Research Letters, 42, 7825–7834, 2015.

Löhnert, U. and Crewell, S.: Accuracy of Cloud Liquid Water Path from Ground-Based Microwave Radiometry 1. Dependency on Cloud Model Statistics, Radio Sci., 38, 8041, https://doi.org/10.1029/2002RS002654, 2003.

Nuijens, L., Serikov, I., Hirsch, L., Lonitz, K., and Stevens, B.: The distribution and variability of low-level cloud in the North Atlantic trades,
505 Quarterly Journal of the Royal Meteorological Society, 140, 2364–2374, 2014.

Nuijens, L., Medeiros, B., Sandu, I., and Ahlgrimm, M.: The behavior of trade-wind cloudiness in observations and models: The major cloud components and their variability, Journal of Advances in Modeling Earth Systems, 7, 600–616, 2015.

Reiche, C. H. and Lasher-Trapp, S.: The minor importance of giant aerosol to precipitation development within small trade wind cumuli observed during RICO, Atmospheric research, 95, 386–399, 2010.

510 Romps, D. M.: Exact Expression for the Lifting Condensation Level, Journal of the Atmospheric Sciences, 74, 3891 – 3900, https://doi.org/10.1175/JAS-D-17-0102.1, 2017.

Schimmel, W., Kalesse-Los, H., Maahn, M., Vogl, T., Foth, A., Garfias, P. S., and Seifert, P.: Identifying cloud droplets beyond lidar attenuation from vertically-pointing cloud radar observations using artificial neural networks, Atmospheric Measurement Techniques, https://doi.org/10.5194/amt-2022-149, 2022.

515 Schlemmer, L. and Hohenegger, C.: The formation of wider and deeper clouds as a result of cold-pool dynamics, Journal of the Atmospheric Sciences, 71, 2842–2858, 2014.

Snodgrass, E. R., Di Girolamo, L., and Rauber, R. M.: Precipitation characteristics of trade wind clouds during RICO derived from radar, satellite, and aircraft measurements, Journal of Applied Meteorology and Climatology, 48, 464–483, 2009.

Stevens, B., Bony, S., Brogniez, H., Hentgen, L., Hohenegger, C., Kiemle, C., L'Ecuyer, T. S., Naumann, A. K., Schulz, H., Siebesma, P. A.,
520 Vial, J., Winker, D. M., and Zuidema, P.: Sugar, gravel, fish and flowers: Mesoscale cloud patterns in the trade winds, Quarterly Journal of the Royal Meteorological Society, 146, 141–152, https://doi.org/10.1002/qj.3662, 2019.

Stevens, B., Bony, S., Farrell, D., Ament, F., Blyth, A., Fairall, C., Karstensen, J., Quinn, P. K., Speich, S., Acquistapace, C., et al.: EUREC 4 a, Earth System Science Data, 13, 4067–4119, 2021.

Touzé-Peiffer, L., Vogel, R., and Rochetin, N.: Cold Pools Observed during EUREC4A: Detection and Characterization from Atmospheric
525 Soundings, Journal of Applied Meteorology and Climatology, 61, 593–610, https://doi.org/10.1175/JAMC-D-21-0048.1, 2022.

Tridon, F., Battaglia, A., and Watters, D.: Evaporation in action sensed by multiwavelength Doppler radars, Journal of Geophysical Research: Atmospheres, 122, 9379–9390, 2017.

Tukiainen, S., O'Connor, E., and Korpinen, A.: CloudnetPy: A Python package for processing cloud remote sensing data, J. Open Source Softw., 5, 2123, https://doi.org/10.21105/joss.02123, 2020.

530 Vogel, R., Konow, H., Schulz, H., and Zuidema, P.: A climatology of trade-wind cumulus cold pools and their link to mesoscale cloud organization, Atmospheric Chemistry and Physics, 21, 16 609–16 630, https://doi.org/10.5194/acp-21-16609-2021, 2021.

Vogl, T., Maahn, M., Kneifel, S., Schimmel, W., Moisseev, D., and Kalesse-Los, H.: Using artificial neural networks to predict riming from Doppler cloud radar observations, Atmospheric Measurement Techniques, 15, 365–381, https://doi.org/10.5194/amt-15-365-2022, 2022.

Witthuhn, J., Röttenbacher, J., and Kalesse-Los, H.: Virga-Sniffer, https://doi.org/10.5281/ZENODO.7010074, 2022.

535   Xie, X., Evaristo, R., Troemel, S., Saavedra, P., Simmer, C., and Ryzhkov, A.: Radar observation of evaporation and implications for quanti-
      tative precipitation and cooling rate estimation, Journal of Atmospheric and Oceanic Technology, 33, 1779–1792, 2016.